Multiple scattering of electrons in solids and molecules: A cluster-model approach

F. J. García de Abajo,[1,2,*] M. A. Van Hove,[1,3] and C. S. Fadley[1,3]

[1]*Materials Sciences Division, Lawrence Berkeley National Laboratory, Berkeley, California 94720*
[2]*Centro Mixto CSIC-UPV/EHU, San Sebastián, Spain*
[3]*Department of Physics, University of California, Davis, California 95616*

A method for the simulation of electron scattering and diffraction in solids and molecules within the cluster approach is presented with explicit applications to photoelectron diffraction, electron scattering in molecules, and low-energy electron diffraction. No approximations are made beyond the muffin-tin model, and, in particular, an exact representation of the free-electron Green function is used. All multiple-scattering paths are accounted for up to an order of scattering that ensures convergence. The method relies upon a convenient separation of the free-electron Green function in rotation matrices and translations along the z axis, which greatly reduces the computation time and storage demand. The evaluation of the multiple-scattering expansion is implemented using the fully convergent recursion method, which permits one to perform an iterative refinement of the final-state wave function, as expressed in the basis set of spherical harmonics attached to each atom of the cluster. Examples are offered in which the direct multiple-scattering expansion and the more elaborated simultaneous relaxation method fail to converge, whereas the recursion method leads to convergence. The computation time needed by the resulting computer program of electron diffraction in atomic clusters to determine the self-consistently scattered wave function is proportional to $N^2(l_{max}+1)^3$, where N is the number of atoms in the cluster and l_{max} is the maximum angular momentum for which the scattering phase shifts take non-negligible values. Within this method it is possible to establish that in practical cases $N > 1000$ might be needed for a convergence of the cluster size, although the angular averaging inherent in many experiments may reduce this. The recursion method was also modified to reduce the effort in computing angular distributions of photoelectrons and low-energy diffracted electrons, which now require negligible time for each angle of emission once the wave function has been determined for a given electron energy. Angle and energy distributions of core-level photoemission, elastic scattering of electrons from a free molecule, and low-energy electron diffraction in large-unit-cell surfaces are calculated.

I. INTRODUCTION

Multiple elastic scattering (MS) plays a central role in the description of electron transport inside solids and molecules in different experimental spectroscopies like photoelectron diffraction (PD),[1–3] low-energy electron diffraction (LEED),[4,5] Auger electron diffraction (AED),[6] x-ray-absorption fine structure (XAFS),[7] and related techniques.

Various approximations are customarily employed to efficiently calculate MS effects. For relatively high electron energies like most of the ones considered in this work (>50 eV above the Fermi level), electron scattering is rather insensitive to the outermost region of the atomic potentials that make up the solid or molecule. Therefore, the atomic potentials can be well approximated by spherically symmetric muffin-tin potentials.[4] In addition, inelastic scattering is usually treated in a phenomenological way via a complex optical potential, or equivalently, inelastic mean free paths.[4]

Two different categories of computational schemes can be distinguished, depending on the use made of the symmetry of the atomic structure in the case of solids: layer-by-layer methods and cluster methods. The former were primarily developed in the context of LEED, and take advantage of the fact that the atoms of an oriented crystal are disposed in layers parallel to the surface, resulting in remarkably efficient algorithms for the transport between layers.[4,8–10] The latter do not require any sort of long-range order, and can be applied to other classes of problems.[11–17]

In particular, when translational crystal symmetry is broken due to either the presence of randomly distributed adsorbates and defects or a localized character of the electron source as in the case of PD and AED, cluster models provide a natural approach for simulating MS effects that is suggested by the fact that excited electrons cannot travel large distances in real solids without suffering inelastic losses, so that the region which actually contributes to the emission of elastically scattered electrons defines a finite cluster surrounding the adsorbate, defect, or emitter.[11–17] This approach is also suitable for dealing with similar scattering phenomena in adsorbed or free molecules.

A hybrid model consisting of treating MS within a cluster formed by concentric spherical shells was proposed by Pendry[18] and implemented by Saldin and co-workers[19–21] to simulate x-ray-absorption near-edge structure,[19] LEED,[20] AED, and PD.[21] This method can in fact be advantageous in LEED calculations when large surface unit cells are considered.[20]

The more straightforward cluster approach adopted in the present work was extensively employed in the past within a single-scattering approximation, and it has been found to reproduce qualitatively, and in several respects quantitatively, many of the experimental features in both XAFS (Refs. 7 and 22) and PD.[2,6,23] However, higher orders of MS are needed to improve accuracy and structural analyses.[24] For

example, by interpreting the terms of the MS series as paths that the electron follows connecting atoms in the cluster in all possible ways,[25] characteristic MS effects like forward focusing and defocusing along rows of atoms have been discerned in PD experiments.[24]

A basis set suited to describe the electron wave function is provided by spherical harmonics and spherical Bessel functions attached to each atom of the cluster. This incorporates curved-wave effects in a natural way. Unfortunately, the propagation of these functions between cluster atoms is computationally very demanding.[26,27,4] Since no intensive use of crystal symmetry is made in cluster models, further approximations have been introduced in the past in order to make feasible the calculation of the MS series.[28–37,2,7,6,11,13–15,21,22]

In the high-energy limit, the propagation reduces to plane-wave factors (hence the name ''plane-wave approximation''), and each term in the MS series becomes a product of scattering amplitudes.[7] Different expansions of the propagated wave function in the finite region centered around each cluster atom lead to the so-called small-atom approximations.[33,11] Among these, the point-scattering approximation goes beyond the plane-wave approximation by multiplying the scattering amplitude by appropriate curved-wave factors.[35]

As the experimental resolution increases, more accurate theoretical analyses become necessary. These are complicated by the fact that the number of multipole terms that are needed rises rapidly with increasing electron energies. The maximum of the significant angular momentum quantum numbers scales roughly as $l_{max} \sim k r_{mt}$, where k is the electron momentum and r_{mt} is the muffin-tin radius of the scatterers. Upon inspection of actual calculations, l_{max} is of the order of 5–20 for electron energies in the range 50–700 eV. Since the number of different multipole components (l,m) used to describe the electron wave function around each atom is $(l_{max}+1)^2$, the aforementioned propagation between each pair of atoms involves multiplication by propagation matrices, requiring $(l_{max}+1)^4$ complex products.

On the other hand, the number of atoms N needed in a cluster to reach convergence is also important in the evaluation of the computational demand of the problem. This number scales as the cube of the electron inelastic mean free path (imfp), λ_i. We estimate N as the number of sites of a simple cubic lattice of lattice constant 2.5 Å that are contained in a sphere of radius $1.5\lambda_i$. The dependence of the universal imfp curve on the electron energy must be also allowed for.[38–40] The relation between l_{max} and the electron momentum discussed above has been assumed for a typical muffin-tin radius $r_{mt}=1.25$ Å. In this way, one obtains the relation between N and l_{max} shown in Fig. 1 by the solid curve.

In order to overcome the rapidly-growing computational demand with increasing l_{max}, Rehr and Albers[13] (RA) provided a clever procedure based upon a separable representation of the free-electron Green function that allows one to generalize the scattering amplitudes, substituting them by matrices that describe each scattering event for a given type of atom in such a way that the leading element of each matrix reproduces the point-scattering approximation. Their method, which produces reliable results when keeping only a
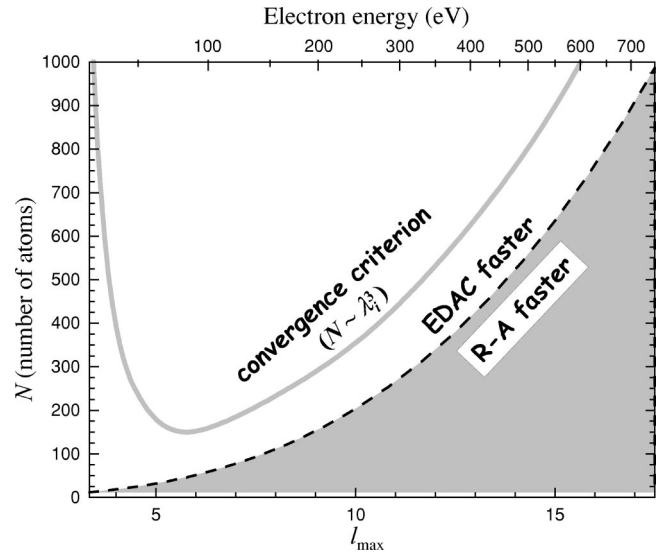

FIG. 1. Minimum criteria for convergence on cluster size and angular momenta in multiple scattering calculations (solid curve) and relative speeds of the present EDAC method versus the second-order Rehr-Albers (RA) separable representation (broken curve). Criteria are expressed in terms of the number of atoms N as a function of the maximum angular-momentum quantum number l_{max}. The value of N for which convergence is achieved (solid curve) is estimated as the number of atoms contained within a sphere of radius equal to 1.5 times the universal inelastic mean free path λ_i, assuming an average nearest-neighbor separation of 2.5 Å. λ_i depends upon the electron momentum k, which is in turn related to l_{max} via $l_{max}=k r_{mt}$ for a typical muffin-tin radius of $r_{mt}=1.25$ Å. The number of complex multiplications needed per iteration is $(10/3)N^2(l_{max}+1)^3$ in EDAC and $36N^3$ in the RA representation, and therefore, EDAC requires a shorter computation time as compared with the RA method when $N>0.1(l_{max}+1)^3$ (white area above the broken curve) if all scattering paths are accounted for.

few more relevant elements in those matrices,[13] is particularly suitable to calculate the contribution of different individual electron paths, and it has been implemented for PD calculations by Kaduwela et al.[17] and Chen et al.[41]

Rather than including all possible electron paths, Zabinsky et al.[36] also showed that only a small fraction of all paths contribute significantly to the MS series in XAFS. This permitted them to reduce the total computational effort substantially by only including in the calculation selected paths whose contributions are already non-negligible within the plane-wave approximation. Their approach is very efficient, in particular if the so-called second-order RA separable representation is used, where each scattering event within a given electron path is typically represented by a 6×6 matrix.

More recently, Chen et al.[41] used a similar approach in the case of PD, incorporating an iterative evaluation of the MS expansion within the framework of the RA separable representation.[13] In this approach, the number of complex multiplications per iteration is $36N^3$.

In the present work, the MS expansion is evaluated using an exact representation of the Green-function propagator. An iterative procedure is followed that requires $\approx (10/3)N^2(l_{max}+1)^3$ multiplications per iteration. Wu and

Tong[42] reported a lack of convergence in the exact MS expansion, and claimed that this problem can be overcome by using the simultaneous relaxation method,[43] consisting of both mixing the result of each iteration with that of the previous one and using the updated components of the wave function as they are calculated rather than waiting for a given iteration to be completed. That iteration procedure is compared in the present paper with the Haydock recursion method,[44–46] which was shown to be more robust and to lead to full convergence even in cases where the former fails to converge. In addition, the recursion method results in faster convergence as compared with either the direct MS expansion or the simultaneous relaxation method. These ideas have been implemented in a fully automated computer code for calculating electron diffraction in atomic clusters (EDAC). A similar approach was recently employed in the description of photon scattering in nanostructures.[47] The computational performance of EDAC as compared with the second-order RA method is shown in Fig. 1 (broken curve): the EDAC method is faster outside the shadowed area.

The MS theory is reviewed in Sec. II in a way suitable to be employed within the selected iterative scheme. Further computational details are given in Sec. III. In particular, several iteration methods are discussed, and a modification of the recursion method is introduced to allow one to calculate scattered or emitted electron intensities for multiple directions simultaneously from a single MS calculation (Sec. III A). Moreover, the free-electron propagators are decomposed into rotations and translations along the z axis, resulting in a significant reduction both in time and in storage demand (Sec. III B). Particular examples of application to PD, elastic electron scattering from molecules, and LEED from surface structures with large unit cells are presented in Secs. IV, V, and VI, respectively. Finally, the main conclusions are summarized in Sec. VII.

Atomic units (a.u., i.e., $e = m = \hbar = 1$) will be used from now on, unless otherwise specified. The notation of Messiah[48] for spherical Bessel and Hankel functions, spherical harmonics, and rotation matrices will be adopted.

II. MULTIPLE-SCATTERING THEORY

Let us begin by introducing the standard elements of multiple scattering theory in a Green-function approach. Consider an electron of energy E described by the wave function $\varphi^0(\mathbf{r})$ that satisfies the free-electron Schrödinger equation

$$(H_0 - E)\varphi^0 = 0, \tag{1}$$

where $H_0 = -\nabla^2/2$.

The presence of a solid or molecule introduces a strong perturbation that can be represented by the potential

$$V(\mathbf{r}) = \sum_\alpha V_\alpha(\mathbf{r}),$$

where the sum is extended over atomic positions $\mathbf{R}_\alpha$. Within the muffin-tin model adopted here, each atomic potential V_α vanishes outside a sphere of radius r_{mt}^α (the muffin-tin radius)

centered at $\mathbf{R}_\alpha$. These are nonoverlapping spheres, and $V(\mathbf{r})$ is set to a constant (the muffin-tin zero) in the interstitial region.

The wave function φ that satisfies the full Schrödinger equation $(H_0 + V - E)\varphi = 0$ can be written $\varphi = \varphi^0 + \phi$, where ϕ is the scattered part. Using matrix notation,[49] the latter can be expressed in terms of the atomic-cluster T matrix as

$$\phi = G_0 T \varphi^0, \tag{2}$$

where G_0 is the free-electron propagator that satisfies $(E - H_0)G_0 = 1$, and $k = \sqrt{2E}$ is the electron momentum. Defining the cluster Green function G via $(E - H_0 - V)G = 1$, the T matrix can be written $T = V + VGV$. An implicit dependence on E is understood in these expressions.

The key ingredient of MS theories is the reduction of the T matrix of the cluster to the T_α matrices of the individual muffin-tin potentials V_α. The latter are defined by the self-consistent relation

$$T_\alpha = V_\alpha + V_\alpha G_0 T_\alpha. \tag{3}$$

Following Beeby,[25] T can be written as a series expansion whose terms represent all possible electron scattering paths. More precisely,

$$T = \sum_\alpha \Lambda_\alpha,$$

where

$$\Lambda_\alpha = T_\alpha + \sum_{\beta \neq \alpha} T_\beta G_0 T_\alpha + \sum_{\gamma \neq \beta} \sum_{\beta \neq \alpha} T_\gamma G_0 T_\beta G_0 T_\alpha + \cdots \tag{4}$$

accounts for MS paths in which the first scattering event occurs at atom α and two consecutive scattering events take place always at different atoms of the cluster. From Eq. (4), T can alternatively be defined as

$$T = \sum_\alpha \left(T_\alpha + \sum_{\beta \neq \alpha} \Lambda_\beta G_0 T_\alpha \right)$$

$$= T_{\alpha_0} + \sum_{\beta \neq \alpha_0} (\Lambda_\beta + \Lambda_\beta G_0 T_{\alpha_0}), \tag{5}$$

for any atom α_0.

Inserting Eq. (5) into Eq. (2), the scattered wave reduces to

$$\phi = \sum_\alpha \left(\phi_\alpha^0 + \sum_{\beta \neq \alpha} G_0 \Lambda_\beta \phi_\alpha^0 \right), \tag{6}$$

where

$$\phi_\alpha^0 = G_0 T_\alpha \varphi^0 \tag{7}$$

represents the first-order contribution to MS. The second term on the right-hand side of Eq. (6) can be understood as

the propagation of the results of scattering at atom α to every other atom of the cluster β, followed by subsequent MS starting at the latter.

Some information on the structure of the scattered wave function can be gained by considering explicit expressions for G_0. That is,

$$G_0(\mathbf{r}-\mathbf{r}') = \frac{-1}{2\pi} \frac{e^{ik|\mathbf{r}-\mathbf{r}'|}}{|\mathbf{r}-\mathbf{r}'|}$$

$$= -2k \sum_L h_L^{(+)}(k\mathbf{r}) j_{l-m}(k\mathbf{r}')(-1)^m$$

$$(r > r'), \quad (8)$$

where $h_L^{(+)}(k\mathbf{r}) = i^l h_l^{(+)}(kr) Y_L(\Omega_\mathbf{r})$ represents an outgoing spherical wave, $j_L(k\mathbf{r}') = i^l j_l(kr') Y_L(\Omega_{\mathbf{r}'})$ is a mixture of outgoing and incoming spherical waves that exhibits no net flux into or out of a closed surface containing the origin, $h_l^{(+)}$ is a spherical Hankel function,[48] j_l is a spherical Bessel function, and $L = (l,m)$ labels spherical harmonics Y_L. Since, by virtue of Eq. (3), T_α vanishes outside the muffin-tin sphere α, one finds, using Eqs. (7) and (8), that

$$\phi_\alpha^0(\mathbf{r}) = \sum_L h_L^{(+)}[k(\mathbf{r}-\mathbf{R}_\alpha)]\phi_{\alpha,L}^0 \quad (9)$$

for $|\mathbf{r}-\mathbf{R}_\alpha| > r_{\mathrm{mt}}^\alpha$.[50] Therefore, ϕ_α^0 is a superposition of outgoing spherical waves centered on $\mathbf{R}_\alpha$. Following a similar argument in Eq. (6), the self-consistently scattered wave can be written

$$\phi(\mathbf{r}) = \sum_\alpha \sum_L h_L^{(+)}[k(\mathbf{r}-\mathbf{R}_\alpha)]\phi_{\alpha,L} \quad (10)$$

for $\mathbf{r}$ outside the muffin-tin spheres. Equation (10) states that the scattered wave finds its sources in the muffin-tin spheres, from which it emerges as a combination of outgoing spherical waves.

The propagation of ϕ_α^0 from atom α to atom β, which is needed in the evaluation of Eq. (6), can be performed by using Eq. (9) and the translation formula of spherical harmonics[26,27,4]

$$h_{L'}^{(+)}[k(\mathbf{r}-\mathbf{R}_\beta)] = \sum_L j_L[k(\mathbf{r}-\mathbf{R}_\alpha)]G_{\alpha\beta,LL'}, \quad (11)$$

where

$$G_{\alpha\beta,LL'} = 4\pi \sum_{L''} h_{L''}^{(+)}[k(\mathbf{R}_\alpha-\mathbf{R}_\beta)]$$

$$\times \int d\Omega Y_L(\Omega) Y_{L''}(\Omega) Y_{L'}^*(\Omega).$$

Equation (11) is valid provided that $|\mathbf{r}-\mathbf{R}_\alpha| < |\mathbf{R}_\alpha-\mathbf{R}_\beta|$; this condition is satisfied when $\mathbf{r}$ is contained inside the muffin-tin sphere $\beta \neq \alpha$, and nonoverlapping spheres are considered. It is also convenient to represent G_0 in the basis set of

spherical harmonics attached to each atom of the cluster. Using Eqs. (8) and (11), one finds[26,27,4]

$$G_0(\mathbf{r}-\mathbf{r}') = -2k \sum_{LL'} j_L[k(\mathbf{r}-\mathbf{R}_\alpha)]$$

$$\times j_{l'-m'}[k(\mathbf{r}'-\mathbf{R}_\beta)](-1)^{m'} G_{\alpha\beta,LL'}, \quad (12)$$

and this expression is valid in the present context for $\alpha \neq \beta$, and $\mathbf{r}$ and $\mathbf{r}'$ lying inside different nonoverlapping muffin-tin spheres.

With the help of these expressions, all spatial integrals that are implicit in Eqs. (4) and (6) (see Ref. 49) can be collected in the so-called scattering matrix elements:

$$t_{\alpha,LL'} = -2k \int d\mathbf{r}d\mathbf{r}' j_{l-m}[k(\mathbf{r}-\mathbf{R}_\alpha)]$$

$$\times (-1)^m T_\alpha(\mathbf{r},\mathbf{r}') j_{L'}[k(\mathbf{r}'-\mathbf{R}_\alpha)]. \quad (13)$$

For spherically symmetric potentials, $t_{\alpha,LL'}$ becomes diagonal, and it is given in terms of the scattering phase shifts δ_l^α as[48]

$$t_{\alpha,LL'} = t_{\alpha,l}\delta_{LL'} = \sin\delta_l^\alpha e^{i\delta_l^\alpha} \delta_{LL'}. \quad (14)$$

Finally, using Eqs. (4) and (9)–(13), and identifying coefficients that multiply into the same functions $h_L^{(+)}[k(\mathbf{r}-\mathbf{R}_\alpha)]$, Eq. (6) leads to

$$\tilde{\phi}_\alpha = \tilde{\phi}_\alpha^0 + \sum_{\beta \neq \alpha} t_\alpha G_{\alpha\beta} \tilde{\phi}_\beta^0 + \sum_{\gamma \neq \beta} \sum_{\beta \neq \alpha} t_\alpha G_{\alpha\beta} t_\beta G_{\beta\gamma} \tilde{\phi}_\gamma^0 + \cdots,$$

$$(15)$$

where $\tilde{\phi}_\alpha^0$ and $\tilde{\phi}_\alpha$ denote column vectors of components $\phi_{\alpha,L}^0$ and $\phi_{\alpha,L}$, respectively, $G_{\alpha\beta}$ represents the matrix of components $G_{\alpha\beta,LL'}$, the scattering matrix t_α has components given by Eq. (14), and matrix multiplication involves summation over indices L, L', etc.

III. COMPUTATIONAL PROCEDURE

The time employed in the direct evaluation of Eq. (15) grows exponentially with the number of terms on the right-hand side. However, an iterative procedure makes it feasible to evaluate the MS series until convergence is achieved, as discussed below in Sec. III A,[41,42,47] where several iteration methods are examined in connection with the solution of that equation, including a modification of the recursion method that allows us to calculate intensities simultaneously for many angles in the far electron field from a single MS calculation.

An exact representation of the free electron Green function is used in the present work, and this is made possible in part thanks to the saving in both computation time and storage demand achieved through the method introduced in Sec. III B: decomposition of the Green function into elementary rotations and translations while keeping track of the latter, so

that they are not unnecessarily re-calculated during the full MS evaluation.

A. Iterative solution of the MS series

It is easy to see that the sum of the first $n+1$ terms on the right-hand side of Eq. (15), $\tilde{\phi}_\alpha^n$, obeys the recurrence relation

$$\tilde{\phi}_\alpha^n = \tilde{\phi}_\alpha^0 + t_\alpha \sum_{\beta \neq \alpha} G_{\alpha\beta} \tilde{\phi}_\beta^{n-1} \quad (n > 0). \tag{16}$$

That is, the difference between $\tilde{\phi}_\alpha^n$ and $\tilde{\phi}_\alpha^{n-1}$ is just the nth sum on the right-hand side of Eq. (15). Each term in that sum contains n products by matrices t_α, that is, it can be interpreted as the contribution of paths along which the electron undergoes n atomic-scattering events.

Taking the $n \to \infty$ limit in Eq. (16), one finds

$$\tilde{\phi}_\alpha = \tilde{\phi}_\alpha^0 + t_\alpha \sum_{\beta \neq \alpha} G_{\alpha\beta} \tilde{\phi}_\beta. \tag{17}$$

The direct inversion of Eq. (17), sometimes called giant-matrix inversion, is prohibitive in many cases, since it requires performing $\sim N^3(l_{max}+1)^6$ complex products. However, this has been carried out by some authors for small values of N and l_{max},[51,52] and is also commonly used within individual layers in a surface with small number of atoms per surface unit cell.[4,5] Three different iterative techniques have been used and compared in the present work to evaluate Eq. (15): (a) direct Jacobi iteration; (b) simultaneous relaxation,[43] previously used in this context;[42] and (c) the Haydock recursion method.[44–46]

(a) Direct Jacobi iteration. This method is based upon the iterative evaluation of Eq. (16). Starting with $\tilde{\phi}_\alpha^0$, each iteration of Eq. (16) leads to the next order of scattering, and this procedure has to be carried out until convergence is achieved. Substituting $\phi_{\alpha,L}^n$ for $\phi_{\alpha,L}$ in Eq. (10), one obtains the approximate wave function calculated up to order n of MS. Since the wave-function coefficients $\phi_{\alpha,L}$ span a space of dimension $(l_{max}+1)^2 N$, Eq. (16) can also be regarded as the power series inversion formula $1/(1-X)|\phi\rangle = (1 + X + X^2 + \cdots)|\phi\rangle$, where X is a matrix that operates on that space, defined in terms of t_α and $G_{\alpha\beta}$, and $|\phi\rangle$ is the vector of coefficients $\phi_{\alpha,L}$. Unfortunately, when any of the eigenvalues of X has a magnitude larger than 1, this expansion series fails to converge. This problem was already discussed in the context of LEED (Ref. 9) and PD.[42] Faster convergent schemes can be found that do not require an extra computational effort, at the price of dismissing the intuitive physical picture of going to the next order of scattering with each iteration step. This is the case of the simultaneous relaxation method and the recursion method discussed next.

(b) Simultaneous relaxation (SR) method. This consists of using the latest values of $\tilde{\phi}_\alpha^n$ as soon as they are calculated. In addition, the result obtained from its iteration is mixed with the previous result to improve convergence. Then the iteration formulas become
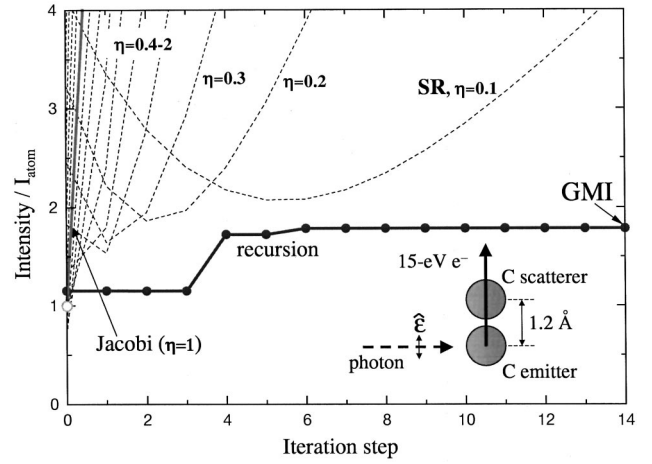

FIG. 2. C $1s$ photoemission intensity in a cluster formed by two carbon atoms separated by 1.2 Å as a function of iteration step. The incoming light is linearly polarized with the polarization vector parallel to the interatomic axis. The emission occurs in the forward-scattering direction (see the inset). The electron energy is 15 eV. Results obtained from different iteration methods are compared: the recursion method of this work (solid circles), which converges rapidly to the exact result derived via giant-matrix inversion (GMI); the direct Jacobi iteration (open circles), for which the number of iteration steps equals the scattering order; and the simultaneous relaxation (SR) method (Refs. 42 and 43) for various values of the relaxation parameter η (thin broken curves). The intensity has been normalized to that of an isolated C atom.

$$\tilde{\phi}_\alpha''^n = \tilde{\phi}_\alpha^0 + t_\alpha \sum_{\beta \neq \alpha} G_{\alpha\beta} \tilde{\phi}_\beta'^n$$

and

$$\tilde{\phi}_\alpha^n = \eta \tilde{\phi}_\alpha''^n + (1 - \eta) \tilde{\phi}_\alpha^{n-1},$$

where $\tilde{\phi}_\beta'^n = \tilde{\phi}_\beta''^n$ for $\beta < \alpha$ and $\tilde{\phi}_\beta'^n = \tilde{\phi}_\beta^{n-1}$ otherwise, and η is a mixing parameter typically adjusted in the range $0 < \eta < 2$ in order to accelerate convergence. For $0 < \eta < 1$ one has what is termed underrelaxation.[43]

(c) Modified recursion method. With the notation of point (a) above, Eq. (17) can be written $|\phi\rangle = (\lambda - X)^{-1}|\phi^0\rangle$ ($\lambda = 1$). The relevant magnitude in which we are interested is the electron current at the detector, which is proportional to $|\langle f|\phi\rangle|^2$ with a suitable definition of the final detected wave function in a given direction $\langle f|$ (see, e.g., Sec. IV below). Haydock's recursion method[44,46] permits one to obtain this matrix element by iterative refinement. Here λ plays the same role as the energy in calculations of solid ground-state properties.[45,46] Although we are only interested in the value $\lambda = 1$ in the present case, the recursion method is advantageous because it is fully convergent for any matrix X. Actually, it produces rigorously exact values when the iteration is carried out $(l_{max}+1)^2 N$ times, although convergence is achieved much earlier, typically in less than 20 iterations in the examples presented in the present work.

In many cases, one is interested in calculating angular distributions of emitted or scattered electrons (e.g., in Fig. 3).
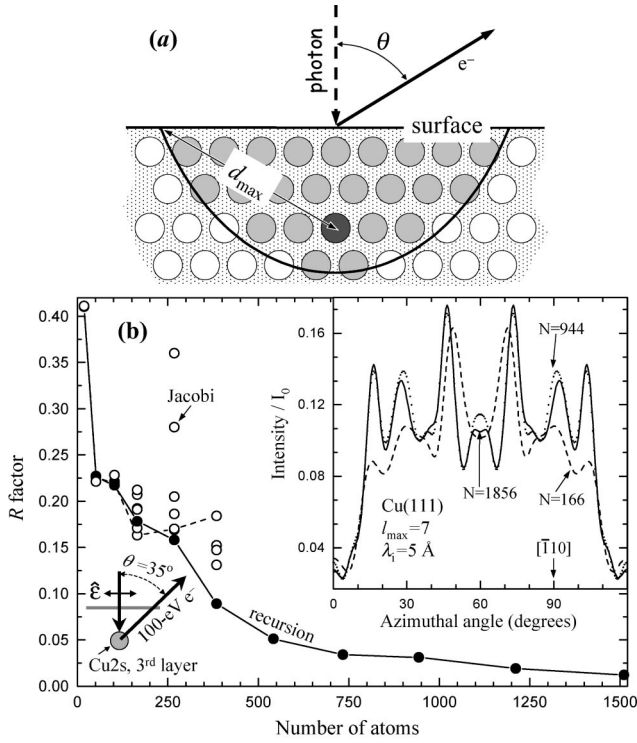
FIG. 3. (a) Schematic representation of the cluster used in photoelectron diffraction calculations. Only atoms whose sum of distances to the emitter (darkest atom) and to the surface is smaller than d_{max} are included in the calculation (gray atoms). This criterion leads to a parabolic surface with the focus coinciding with the emitter. (b) R-factor [Eq. (34)] variation with the number of atoms N for Cu $2s$ photoemission from the third layer of a Cu(111) surface. Azimuthal scans have been considered with a polar angle of emission of 35°, a photoelectron energy of 100 eV, and p-polarized light under normal incidence conditions, as shown schematically in the lower left corner of the figure. The inset shows the intensity as a function of azimuthal angle for various cluster sizes, as indicated by labels, normalized to that of the direct emission without inelastic attenuation.

Unfortunately, the recursion method requires carrying out the MS iteration procedure for each direction of emission (i.e., for each $\langle f|$). Here we have modified the recursion method so that it allows one to obtain intensities for various directions of emission with a single MS calculation, provided one stores the moments $\mu_n = \langle f|X^n|\phi^0\rangle$ for each $\langle f|$ and each iteration step n. Our modified method is based upon the double recurrence

$$|\alpha_{p+1}\rangle = [(X^\dagger - a_p^*)|\alpha_p\rangle - b_p^*|\alpha_{p-1}\rangle]/b_{p+1}^* \quad (18)$$

and

$$|\beta_{q+1}\rangle = [(X - a_q)|\beta_q\rangle - b_q|\beta_{q-1}\rangle]/b_{q+1}, \quad (19)$$

where the starting values are $|\alpha_{-1}\rangle = |\beta_{-1}\rangle = 0$, $|\alpha_0\rangle = |f\rangle/\sqrt{\mu_0^*}$, and $|\beta_0\rangle = |\phi^0\rangle/\sqrt{\mu_0}$, and a_n and b_n are complex numbers. Upon inspection, one can easily prove that

$$\langle \alpha_i|\beta_j\rangle = \delta_{ij} \quad (20)$$

if one chooses

$$a_n = \langle\alpha_n|X|\beta_n\rangle \quad (21)$$

and b_{p+1} such that $\langle\alpha_{p+1}|\beta_{p+1}\rangle = 1$. Haydock's recursion method is recovered in the special case where $X = X^\dagger$ and $|f\rangle = |\phi^0\rangle$.[44] These recurrences share in common with Haydock's method the property that the matrix of components $\langle\alpha_i|X|\beta_j\rangle$ is tridiagonal, as can be seen from Eqs. (18), (19), and (20), and this permits writing the desired matrix element as the continued fraction[44]

$$\langle f|(\lambda - X)^{-1}|\phi^0\rangle = \cfrac{\langle f|\phi^0\rangle}{\lambda - a_1 - \cfrac{b_1^2}{\lambda - a_2 - \cfrac{b_2^2}{\lambda - a_3 - \cdots}}}. \quad (22)$$

Different terminations of the iteration procedure have been proposed,[44] but in the present context, our results are quite insensitive to the particular choice.

Rather than directly evaluating these recurrences, an equivalent recurrence can instead be constructed using the quantities

$$I_{pq}^n = \langle\alpha_p|X^n|\beta_q\rangle.$$

Multiplying Eq. (19) by $\langle\alpha_p|X^n$, one finds

$$I_{pq+1}^n = [I_{pq}^{n+1} - a_q I_{pq}^n - b_q I_{pq-1}^n]/b_{q+1}, \quad (23)$$

and, similarly, from Eq. (18),

$$I_{p+1,q}^n = [I_{pq}^{n+1} - a_p I_{pq}^n - b_p I_{p-1,q}^n]/b_{p+1}. \quad (24)$$

Moreover, Eq. (21) can be recast as

$$a_p = I_{p,p}^1, \quad (25)$$

and the normalization factor b_{p+1} becomes

$$b_{p+1} = \sqrt{I_{pp}^2 - a_p^2 - b_p^2}. \quad (26)$$

Now a_p and b_p, and therefore also Eq. (22), can be evaluated using Eqs. (23), (24), (25), and (26) recursively with the starting values $I_{00}^n = \mu_n/\mu_0$ and $I_{p,-1}^n = I_{-1q}^n = 0$. The relevance of this procedure is that it permits calculating the matrix element [Eq. (22)] directly from the moments μ_n, which are in turn obtained from a single MS calculation for as many $\langle f|$'s as desired.

Comparisons of rapidity of convergence using these iteration methods are offered in Figs. 2, 3, and 4 for PD, and in Fig. 7 for electron scattering. The results are discussed in more detail in Secs. IV and V.

An important point about the iteration methods just described is that the number of products of scattering matrices t_α per iteration is N in all of them, whereas the number of $G_{\alpha\beta}\tilde{\phi}_\beta$ products is $N(N-1)$. Therefore, in realistic clusters, where $N > 100$ (see Fig. 1), no substantial relative increase in computational effort is introduced if one goes beyond the commonly used spherical muffin-tin approximation, that is, if nondiagonal scattering matrices like those needed to represent nonspherical potentials[53–55] (e.g., in photoelectron dif-
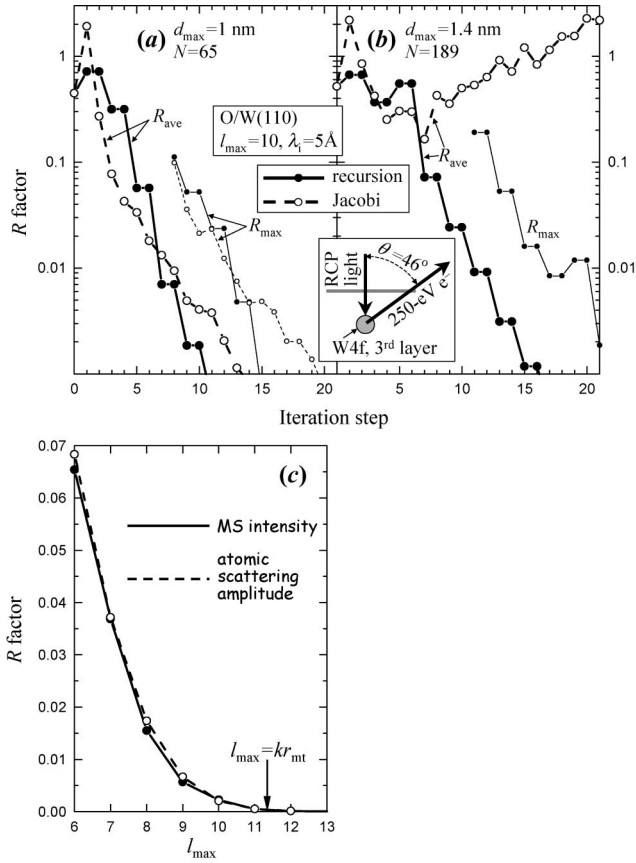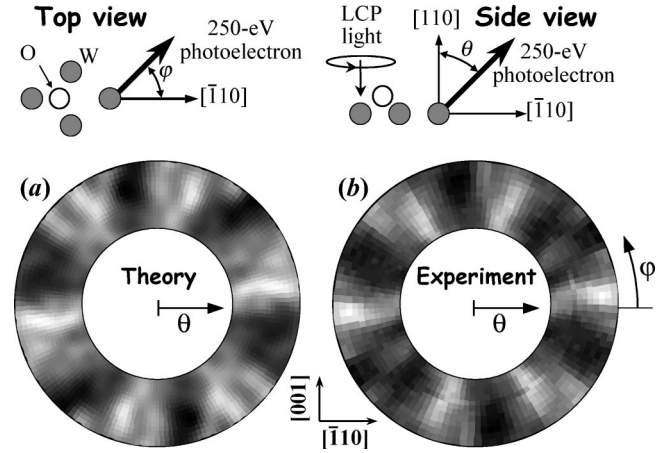
FIG. 5. W $4f$ photoemission intensity as a function of the polar direction of emission for a W(110) surface covered with one monolayer of 1×1 O and illuminated with left circularly polarized light (Ref. 59). Represented is $[I(\theta,\varphi) - I_0(\theta)]/I_0(\theta)$, where $I_0(\theta)$ is the average of the intensity over azimuthal angles. The photoelectron energy is 250 eV. The emission takes place from the top-most (oxide) W layer. Dark regions correspond to high intensity. (a) EDAC calculation for a cluster consisting of $N = 393$ atoms ($d_{max} = 18$ Å). The position of the oxygen is shown schematically in the inset. An average over the two symmetry-equivalent positions of the oxygen has been performed. The direction of normal emission corresponds to the center of the figure, and the polar angle θ is proportional to the distance to that point (the range actually plotted is $46° \leqslant \theta \leqslant 63.5°$). (b) Experimental results taken from Ref. 59.

FIG. 4. (a) R-factor variation with scattering order for azimuthal scans of W $4f$ photoemission from a W(110) surface covered with one monolayer of 1×1 O (Ref. 59). The emitter is taken to be in the third W layer, the photoelectron is emitted with an energy of 250 eV and a polar angle of 46°, and the incident light is circularly polarized and coming perpendicular to the surface (see the inset). The cluster consists of $N = 65$ atoms [$d_{max} = 1$ nm; see Fig. 3(a)]. Results derived from the recursion method (solid curves and circles) are compared with those obtained using direct Jacobi iteration (broken curves and open circles). Thick and thin curves show R-factor values according to the definitions of Eqs. (34) and (35), respectively (i.e., the relative value of the average deviation and the maximum deviation, respectively). (b) Same as (a) for $N = 189$ atoms [$d_{max} = 1.4$ nm; see Fig. 3(a)]. (c) R-factor variation with l_{max} under the same conditions as in (a) for $d_{max} = 1.2$ nm (solid curve and solid circles). The variation of the R factor for the atomic scattering amplitude as defined by Eq. (36) is shown by the broken curve and open circles. Also shown is the expected l_{max} value based on the simple criterion of $l_{max} = kr_{mt}$.

fraction in oriented molecules[56]) or spin-orbit coupling[53] are considered. Since most of the computational effort is invested in products by $G_{\alpha\beta}$ matrices (vector addition takes a negligible time), we have devoted Sec. III B to a description of how to minimize their computational cost.

B. Optimization of products of Green functions

Following previous authors,[26,13,14] the Green function $G_{\alpha\beta}$ that propagates a free electron along an interatomic bond vector $\mathbf{d}_{\alpha\beta} = \mathbf{R}_{\alpha} - \mathbf{R}_{\beta}$ will be expressed in terms of the
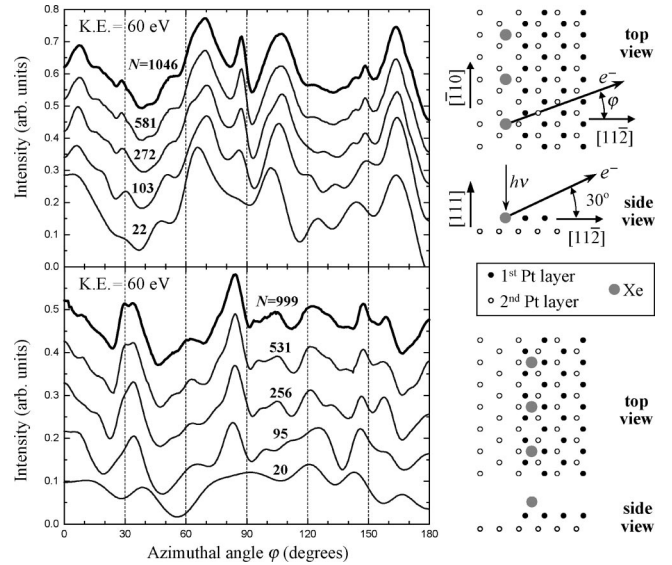

FIG. 6. Azimuthal dependence of the photoemission intensity from s levels of a row of Xe atoms adsorbed near a step in a Pt(111) surface. Top part: the Xe atom is on the lower terrace at the step edge. Bottom part: the Xe atom is on the upper terrace. In all cases, the Xe atoms are located in Pt continuation sites. (See the schematic representations on the right-hand side.) The photoelectron kinetic energy is 60 eV. The electron take-off angle is 30°. The light is unpolarized and incident perpendicular to the terraces.
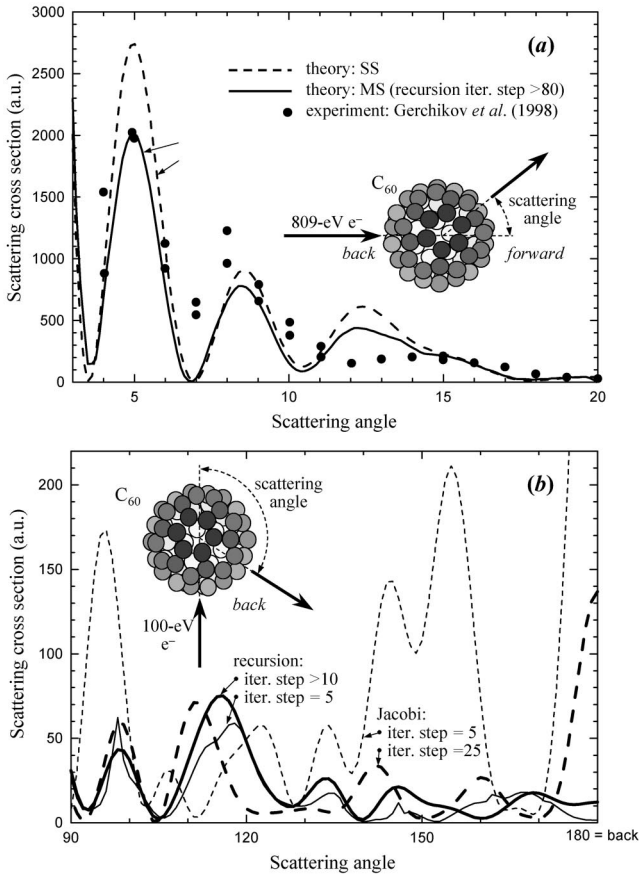
FIG. 7. (a) Scattering probability of 809-eV electrons from C_{60} molecules as a function of scattering angle. Experimental results (circles) taken from Ref. 64 are compared with single-scattering (broken curve) and multiple-scattering (solid curve) calculations. An average over molecular orientations has been performed. (b) Scattering probability of 100-eV electrons from C_{60} molecules as a function of scattering angle calculated for various iteration steps (see labels) using the recursion method (solid curves) and direct Jacobi iteration (broken curves).

propagator along the z axis by using rotation matrices $R_{mm'}^{(l)}(\alpha\beta\gamma)$, where $(\alpha\beta\gamma)$ are the corresponding Euler angles.[48] In a first step, the bond vector $\mathbf{d}_{\alpha\beta}$ is rotated onto the z axis by applying the matrix[13,48]

$$R_{\alpha\beta,LL'} = \delta_{ll'} R_{mm'}^{(l)}(0,\theta,\pi-\varphi), \qquad (27)$$

where (θ,φ) are the polar angles of $\mathbf{d}_{\alpha\beta}$. Then the electron is propagated along the bond vector, now directed along the z axis, and for which the Green function reduces to

$$G_{\alpha\beta,LL'}^z = \delta_{mm'} \sqrt{4\pi} \sum_{l''} \sqrt{2l''+1}\, i^{l''} h_{l''}^{(+)}(kd_{\alpha\beta})$$

$$\times \int d\Omega\, Y_{lm}(\Omega) Y_{l''0}(\Omega) Y_{l'm}^*(\Omega). \qquad (28)$$

Finally, the bond vector is rotated back to the original position, and one finds[13,41]

$$G_{\alpha\beta} = R_{\alpha\beta}^{-1} G_{\alpha\beta}^z R_{\alpha\beta}. \qquad (29)$$

A recurrence relation has been reported that permits evaluating Eq. (28) efficiently.[15] The rotation matrices can be in turn decomposed into azimuthal and polar rotations as[48]

$$R_{mm'}^{(l)}(0,\theta,\pi-\varphi) = R_{mm'}^{(l)}(0,\theta,0)(-1)^{m'} e^{i\varphi m'}.$$

This decomposition of the Green function permits us to reduce both (i) the storage required to evaluate the MS series and (ii) the computational effort.

(i) A significant reduction in memory demand can be accomplished if the coefficients of each polar rotation $R_{mm'}^{(l)}(0,\theta,0)$, each azimuthal rotation $(-1)^{m'} e^{i\varphi m'}$, and each propagation along a bond distance $G_{\alpha\beta,LL'}^z$ are computed and stored once and for all the first time that they are encountered during the full calculation. Since actual clusters on which MS calculations are to be performed possess in general a certain degree of symmetry, the total number of different bond distances and bond polar angles is considerably reduced as compared with the total number of bond vectors. To illustrate this, let us take the example of a simple-cubic-lattice cube of side p in units of the lattice constant; this cluster contains p^3 atoms and $(2p-1)^3-1$ different bond vectors, a number that has to be compared with at most $3p^2$ bond distances, since the square of the distance between any pair of atoms has to be equal to an integral number, and the distance between opposite corners is $\sqrt{3}p$. A better estimate for this case results in $\approx 1.8p^2$ different bond distances.

(ii) For a given maximum value of the angular momentum number $l_{\max}$, the dimension of each vector $\tilde{\phi}_\alpha$ is $(l_{\max}+1)^2$, so that every matrix-vector product $G_{\alpha\beta}\tilde{\phi}_\beta$ involves $(l_{\max}+1)^4$ complex multiplications. However, all of the three matrices that appear on the right-hand side of Eq. (29) are sparse, as can be seen from Eqs. (27) and (28). A detailed inspection leads to the conclusion that only $\approx (10/3)(l_{\max}+1)^3$ complex multiplications are needed to evaluate the product $G_{\alpha\beta}\tilde{\phi}_\beta$ when $G_{\alpha\beta}$ is decomposed as shown in Eq. (29). This is a factor of $\approx 3l_{\max}/10$ smaller than the direct matrix-vector product.

Further reduction in computational and storage demand can be achieved if symmetry relations for the Green function and the rotation matrices[48] are used (e.g., $G_{\alpha\beta,lm,l'm}^z = G_{\alpha\beta,l'-m,l-m}^z$). The overall reduction in storage demand comes ultimately from the decomposition of the Green functions, as shown in this section, so that many of the rotation matrices and propagators along the z axis (all of them sparse matrices) are shared by Green functions connecting different pairs of cluster atoms. In the examples reported below, the time needed to calculate and store the matrices defined in Eqs. (27) and (28) is negligible compared with the time spent in the iterative evaluation of Eq. (16).

C. Electron attenuation, temperature effects, and surface barrier

The effect of electron inelastic scattering is easily accounted for in a phenomenological way by multiplying the

propagator $G_{\alpha\beta}^z$ of Eq. (28) by an exponentially decaying function of the bond distance, $\exp(-d_{\alpha\beta}/2\lambda_i)$, where λ_i is the inelastic electron mean free path,[38–40] and the 1/2 factor reflects the fact that this function goes inside the wave function rather than the electron probability. Also, the propagation from each atom to the detector has to be accompanied by a corresponding exponential attenuation that takes care of the part of the path contained inside the cluster (or below the surface in the case of a solid sample, of which the cluster represents just a part). Inelastic scattering, together with MS, reduces the scattering range, making LEED and PD excellent surface analysis techniques. In the case of core-level photoemission, the photoelectrons ejected from a solid or molecule thus provide information only on the vicinity of the ionized atom, and features coming from the interaction with distant atoms are attenuated by a finite inelastic mean free path. The effect of thermal vibrations has been incorporated as is generally done in LEED analyses[4] by means of temperature-dependent phase shifts that take into account an average displacement of the cluster atoms in their thermal motion.

Refraction at the surface barrier or inner potential V_0 requires correlating the direction of emission as seen from inside a solid with the actual direction of detection outside of it. The relation between these two is easily obtained by invoking conservation of the electron momentum parallel to the surface, and taking into account the loss of electron kinetic energy in the motion normal to the surface. A transmission factor is also needed,[57] especially for nearly grazing emission (i.e., when the normal kinetic energy is only a few eV above the vacuum threshold). Diffraction of electron components reflected back from the surface has been neglected, although we note that this can play a very important role at very low normal kinetic energies.

We now apply this general methodology to three important classes of experiment: core-level photoelectron diffraction, elastic electron scattering from molecules, and low-energy electron diffraction at surfaces.

IV. CORE-LEVEL PHOTOELECTRON DIFFRACTION

In this section, our methods are applied to the case of photoelectron diffraction. Describing the interaction with the external radiation $H_{\rm rad}$ to first order, the perturbed part of the time-dependent wave function $\phi(\mathbf{r})\exp(-iEt)$ is given by

$$\phi(\mathbf{r}) = \int d\mathbf{r}' \, G(\mathbf{r},\mathbf{r}') H_{\rm rad}(\mathbf{r}') \phi_i(\mathbf{r}'), \qquad (30)$$

where $\phi_i(\mathbf{r})$ is the initial-state core-electron wave function, and $G(\mathbf{r},\mathbf{r}')$ is the cluster Green function discussed in Sec. II and evaluated at the final electron energy E. The photoexcitation of a core-level electron in a solid or molecule can be well described within the dipole approximation when the radiation wavelength is much larger than the dimensions of the initial core-electron state, in which case one can take $H_{\rm rad} = C\hat{\boldsymbol{\epsilon}} \cdot \mathbf{r}$, where $\hat{\boldsymbol{\epsilon}}$ is the photon-polarization unit vector and C is a normalization constant.

In matrix notation, expressing G in terms of T as $G = G_0 + G_0 T G_0$ and using Eq. (5), Eq. (30) becomes

$$\phi = G_0 H_{\rm rad} \phi_i + G_0 T_{\alpha_0} G_0 H_{\rm rad} \phi_i + \sum_{\beta \neq \alpha_0} G_0 \Lambda_\beta G_0 H_{\rm rad} \phi_i$$

$$+ \sum_{\beta \neq \alpha_0} G_0 \Lambda_\beta G_0 T_{\alpha_0} G_0 H_{\rm rad} \phi_i,$$

where α_0 is taken to be the emitter. Noting that $G_{\alpha_0} = G_0 + G_0 T_{\alpha_0} G_0$ is the Green function of atom α_0, one finds

$$\phi = G_{\alpha_0} H_{\rm rad} \phi_i + \sum_{\beta \neq \alpha_0} G_0 \Lambda_\beta G_{\alpha_0} H_{\rm rad} \phi_i,$$

which can be compared to Eq. (6) to redefine

$$\phi_\alpha^0(\mathbf{r}) = \delta_{\alpha\alpha_0} C \int d\mathbf{r}' \, G_{\alpha_0}(\mathbf{r},\mathbf{r}') \hat{\boldsymbol{\epsilon}} \cdot \mathbf{r}' \phi_i(\mathbf{r}'). \qquad (31)$$

We are interested in values of $\mathbf{r}$ outside the muffin-tin sphere of the emitter α_0, whereas the integral in Eq. (31) involves $\mathbf{r}'$ inside the muffin-tin sphere (i.e., the region where the core-electron wave function takes non-negligible values). Under these conditions, G_{α_0} can be written as[48]

$$G_{\alpha_0}(\mathbf{r},\mathbf{r}') = -2k\sum_L h_L^{(+)}[k(\mathbf{r}-\mathbf{R}_{\alpha_0})] F_L^*(\mathbf{r}') \exp(i\delta_l^{\alpha_0}), \qquad (32)$$

where $F_L(\mathbf{r}) = i^l F_l(r) Y_L(\Omega_\mathbf{r})$ is a solution of $(H_0 + V_{\alpha_0} - E)F_L = 0$, and F_l is chosen such that it is finite at the origin (the regular solution). Inserting Eq. (32) into Eq. (31) and comparing the result with Eq. (9), one obtains

$$\phi_{\alpha,L}^0 = -2kC\delta_{\alpha\alpha_0} e^{i\delta_l^{\alpha_0}} \langle F_L | \boldsymbol{\epsilon} \cdot \mathbf{r} | \phi_i \rangle,$$

which includes the dipole matrix elements $\langle F_L | \boldsymbol{\epsilon} \cdot \mathbf{r} | \phi_i \rangle$ and phase shifts $\delta_l^{\alpha_0}$ that are well known in the theory of atomic photoelectric cross sections.[48] Finally, the MS coefficients $\phi_{\alpha,L}$ are obtained from $\phi_{\alpha,L}^0$ as explained in Sec. III, and $\phi(\mathbf{r})$ is given by Eq. (10) outside the muffin-tin spheres.

When $\mathbf{r}$ lies at the electron detector (i.e., for r much larger than the interatomic distances of the cluster) we are in the far-field limit, and can approximate $h_L[k(\mathbf{r}-\mathbf{R}_\alpha)] \approx \exp(ikr - i\mathbf{k}_f \cdot \mathbf{R}_\alpha) Y_L(\Omega)/kr$, where $\mathbf{k}_f = k\mathbf{r}/r$ and Ω is the polar direction of $\mathbf{r}$ (i.e., the detector). Therefore, using Eq. (10), the measured electron intensity per unit of solid angle in the far field becomes

$$I(\Omega) = \left| \frac{C}{k} \sum_\alpha e^{-i\mathbf{k}_f \cdot \mathbf{R}_\alpha - \zeta_\alpha/2\lambda_i} \sum_L Y_L(\Omega) \phi_{\alpha,L} \right|^2, \qquad (33)$$

where ζ_α is the distance from atom α to the surface along the direction of emission, and λ_i is the inelastic electron mean free path. In general, comparison with experiments requires performing an incoherent sum over different degenerate initial states and possibly over various emitters α_0.

For PD from atoms on or below a solid surface, and for which the entire (focused) photon beam is intercepted by the sample, the intensity can be given in electrons per steradian per incoming photon by choosing the normalization constant as $|C|^2 = 4\pi k \sigma(\omega/c)/\cos\theta_i$, where ω is the photon energy,

c is the speed of light, θ_i is the polar angle of incidence of the light with respect to the surface normal, and σ is the surface density of emitters equivalent to α_0 (i.e., those of a given layer parallel to the surface).

The present formalism is particularly efficient when calculating photoelectron angular distributions: once the coefficients $\phi_{\alpha,L}$ have been obtained for a given electron energy, the photoelectron intensity for each emission direction is readily calculated using Eq. (33). When using the modified recursion method outlined in Sec. III A, $\langle f | \phi \rangle$ corresponds to the expression inside the modulus in Eq. (33) and the moment n is given by $\mu_n = \langle f | \phi^n \rangle - \langle f | \phi^{n-1} \rangle$, where $\langle f | \phi^n \rangle$ is calculated from the coefficients $\phi_{\alpha L}^n$ obtained in the nth iteration.

The relative performances of the various iteration methods discussed in Sec. III A for calculating PD from a simple sample consisting of two carbon atoms is analyzed in Fig. 2, where the inset illustrates the details of the geometry. This constitutes a severe test of multiple scattering, since the interatomic distance is relatively small. Within the resolution of the figure, the recursion method (solid circles) converges in just six iterations to the result of the exact giant-matrix inversion. In single scattering (SS), that is, at iteration 1, the direct Jacobi iteration (open circles) is already much worse, and subsequent scattering orders clearly show a lack of convergence. Neither is such lack of convergence prevented by using the SR method (broken curves) over a wide range of the relaxation parameter η. The lower the value of η, the slower is the increase in intensity with iteration step, but the lack of convergence remains.

This lack of convergence comes about in MS when the absolute value of any of the eigenvalues of the matrix X discussed in Sec. III A is larger than 1. In a basis set that makes this matrix diagonal, each eigenvalue x_i enters the direct Jacobi MS expansion of $1/(1-X)$ as $1/(1-x_i)=1+x_i+x_i^2+\cdots$, and this expansion is only convergent when $|x_i|<1$. This is a well-known problem in LEED,[4,5] where various schemes have been devised to prevent it, such as renormalized forward scattering[4,5,9] and reverse scattering perturbation.[5,19] The SR method provides a cure in many cases,[42] but it is not sufficiently general, as illustrated by Fig. 2. Instead, the recursion method has a well-established convergent behavior,[44] and therefore, it will be employed from now on unless otherwise specified.

Figure 3(a) shows our choice of the cluster used to represent photoemission from a given atom (darker circle) within a solid surface. The cluster is formed by those atoms contained within a parabolic surface where the emitter coincides with its focus. The parameter d_{max} determines the size of the cluster (see Fig. 3). The parabolic surface comes from the condition that the maximum electron path length inside the solid, where the inelastic attenuation is effective, be at most d_{max} within SS for normal emission.

Convergence with the number of cluster atoms $N \propto d_{max}^3$ is analyzed in Fig. 3(b) for photoemission from a Cu $2s$ level situated on the third layer of a Cu(111) surface and at a polar emission angle of $\theta=35°$. The geometry under consideration is illustrated schematically in the lower left corner of

the figure, and the atoms are again within the paraboloid of Fig. 3(a). Plotted here is the reliability factor, defined as[58]

$$R_{ave} = \frac{\overline{|I^N - I^\infty|}}{\overline{I^\infty}}, \qquad (34)$$

where the average is taken over all azimuthal directions of emission (cf. inset), I^N is the intensity calculated for an N-atom cluster, and I^∞ is actually obtained for $N=1856$. The solid curve and circles correspond to the result obtained from the recursion method, where convergence is achieved in less than 20 iterations. A smooth convergence can be seen in the $N \to \infty$ limit. For $N \approx 160$, which is suggested by Fig. 1 as a convergence criterion for the electron energy under consideration (100 eV), one has $R_{ave}=0.16$. The inset shows azimuthal scans obtained for different cluster sizes, in order to facilitate an understanding of the actual meaning of R_{ave} in terms of curve comparisons. For $N=944$ (dotted curve in the inset), one has $R_{ave}=0.03$ and convergence is already quite good as compared to the $N=1856$ case, although some small discrepancies can still be distinguished in the height of the peaks around 30°, 60°, and 90°, so that over 1000 atoms are needed to obtain convergence within the resolution of the figure. We note, however, that most real experimental situations involve averaging over some finite solid angles, and this can lead to an effective reduction in the cluster size needed.

The open circles in Fig. 3(b) show the reliability factor obtained from the Jacobi method for various scattering orders (5, 9, 13, 17, 21, and 25), where the spread in the position of the circles makes evident a lack of convergence. The latter is more pronounced for larger clusters. In this sense, the Jacobi method has to be regarded as an asymptotic series unable to converge below a certain reliability factor in the present case.

Figures 4(a) and 4(b) show the performance of the recursion method (solid circles, for which only odd iteration orders introduce variations by construction of the method) as compared with that of direct Jacobi iteration (open circles) as a function of iteration step for $4f$ photoemission from the third W layer in a W(110) surface covered with one monolayer of 1×1 O and with an emission angle of 46°.[59] Two different definitions of the reliability factor have been used, based upon either the relative average deviation given by Eq. (34) by substituting N by the iteration step n (R_{ave}, thick curves), or the maximum deviation over the azimuthal scan (thin curves)

$$R_{max} = \frac{\max\{|I^n - I^\infty|\}}{\overline{I^\infty}}, \qquad (35)$$

respectively, where the average is performed over azimuthal scans for a polar angle of emission $\theta=46°$. Both iteration methods show similar convergence behavior for the relatively small cluster of Fig. 4(a), consisting of $N=65$ atoms. However, for the larger cluster of Fig. 4(b) ($N=189$), the Jacobi method fails to converge, whereas the recursion method shows a steady convergent trend.

As pointed out above, the computational cost of EDAC scales as $(l_{max}+1)^3$ with l_{max}. Consequently, it is desirable to have a criterion to limit the value of l_{max} used in actual MS calculations while maintaining the required degree of accuracy. This criterion is provided by the reliability factor for the atomic scattering amplitude f,

$$R_f = \frac{1}{3}\sqrt{\frac{\int d\Omega |f^{l_{max}} - f^{l_{max}=\infty}|^2}{\int d\Omega |f^{l_{max}=\infty}|^2}}, \qquad (36)$$

where the integrals are extended over all scattering directions Ω. Figure 4(c) shows the dependence of R_f on l_{max} for 250-eV electrons scattered on W atoms (open circles) as compared with the reliability factor for MS under the same conditions as in Fig. 4(a) for $N=123$ atoms (solid circles). The latter has been obtained from Eq. (34) by varying l_{max} rather than N for azimuthal scans with polar angle of emission $\theta=46°$. Both Eqs. (34) and (36) are proportional to relative variations of the atomic scattering amplitude, so that one is comparing quantities of the same order of magnitude. Actually, they exhibit a similar behavior with l_{max}, as shown in Fig. 4(c), which indicates that Eq. (36), whose computation requires a negligible time as compared with MS calculations, offers a good estimate of the error that is made when finite values of l_{max} are used, thus providing a criterion to determine the appropriate value of l_{max} before performing actual MS calculations. Similar results are obtained for other values of θ. Interestingly, all angles of scattering enter into the definition of R_f, and this is consistent with the fact that MS in a solid involves a dense set of single scattering angles. Also shown in Fig. 4(c) is the l_{max} value obtained from the simple criterion mentioned earlier ($l_{max}=kr_{mt}$), which is 11.3.

As another PD example, Fig. 5 shows the angular distribution over the upper-hemisphere for W $4f$ photoelectrons coming from the outer W layer of a W(110) surface covered with one monolayer of 1×1 O and illuminated with left circularly polarized (LCP) light under normal incidence, as shown in the insets. The quantity actually plotted is $[I(\theta,\varphi)-I_0(\theta)]/I_0(\theta)$, where I_0 is the average of the intensity over azimuthal angles. In calculating the data displayed in Fig. 5(a), the MS procedure has been carried out only once for all directions of emission, as explained in Sec. III A, thus saving considerable time. Figure 5(a) exhibits reduced symmetry with respect to that expected for W(110) owing to the fact that LCP light is used, and also because the oxygen atoms are displaced with respect to a center of symmetry of the surface (see the schematic top view). Two different domains can also exist on this surface:[59] the one depicted in the insets, and another one with the oxygen lying in a mirror-image symmetry-equivalent W valley. The average over the result obtained from both domains has been performed. The maximum intensity (bright regions) near the [001] azimuthal direction is rotated clockwise, as expected from the use of LCP light and f core levels.[60,61,59] This rotation reproduces very well the available experimental data shown in Fig. 5(b), and taken from Ref. 59.

As a last example of PD, we consider photoemission from atoms near surface steps, where the lack of symmetry makes it difficult to use layer-by-layer methods in simulations, while the cluster approach is perfectly suited for that purpose. Prior x-ray PD experiments on O adsorbed on stepped Cu surfaces indicated, for instance, a high sensitivity to structure via SS calculations.[62] Here we show calculated azimuthal scans of photoelectrons coming from Xe atoms adsorbed near a step on a Pt(111) surface (Fig. 6). The insets on the right-hand side of the figure schematically show the geometry under consideration. Two different possible structures have been studied: one row of Xe atoms located either on the lower terrace (upper part of the figure) or on the upper terrace (lower part), continuing the bulk Pt structure in both cases. Experimental evidence coming from low-energy ion scattering[63] indicates that the lower terrace is the preferred geometry. The results presented in Fig. 6 permit one to conclude that the features exhibited by PD scans would allow one to distinguish between the two possibilities, although no actual experimental data are available for this case. Moreover, at least 100 atoms are needed to obtain the dominant features when the Xe atoms are sitting on the upper terrace. However, strong forward scattering, dominated by nearest neighbors of the emitter, occurs when the Xe atoms are sitting on the lower terrace, and therefore, a 22-atom cluster produces good qualitative results. In both cases, convergence in the fine structure requires approximately 500 atoms.

V. ELASTIC ELECTRON SCATTERING FROM MOLECULES

The scattering of an external electron beam from a molecule represented by an atomic cluster is discussed in this section. The initial electron state of Eq. (1) will be described by a plane wave $\varphi^0(\mathbf{r})=\exp(i\mathbf{k}_i\cdot\mathbf{r})$, which can be expanded in partial waves around each of the cluster atoms, and using Eqs. (7)–(9) and (13), one finds

$$\phi_{\alpha,L}^0 = 4\pi t_{\alpha,l} Y_{l-m}(\Omega_{\mathbf{k}})(-1)^m e^{i\mathbf{k}_i\cdot\mathbf{R}_\alpha - \zeta_\alpha/2\lambda_i}, \qquad (37)$$

where ζ_α has the same meaning as in Eq. (33), with the *surface* now defined as the boundary of the molecular electronic charge distribution. These are the input wave-function coefficients from which one can obtain those of the self-consistent wave function [Eq. (10)], $\phi_{\alpha,L}$, after MS is performed using the methods described in Sec. III. The latter, upon insertion into Eq. (33), permits one to compute the diffracted electron intensity. Choosing $C=1$, Eq. (33) represents the scattering cross section.

This procedure is carried out for C_{60} molecules and 809-eV electrons in Fig. 7(a), where experimental results taken from Ref. 64 are compared with SS calculations (also reported in Ref. 64) and MS calculations represented by broken and solid curves, respectively, as a function of scattering angle. MS results in better agreement for the relative height of the prominent diffraction peaks at around 5° and 8.5°, as compared with the SS analysis.

In order to emphasize the contribution of MS, lower electron energies (100 eV) and a backscattering geometry are considered in Fig. 7(b) for electron scattering by C_{60} mol-

SURFACE STRUCTURE FACTOR

UNIT-CELL ENVELOPE FUNCTION

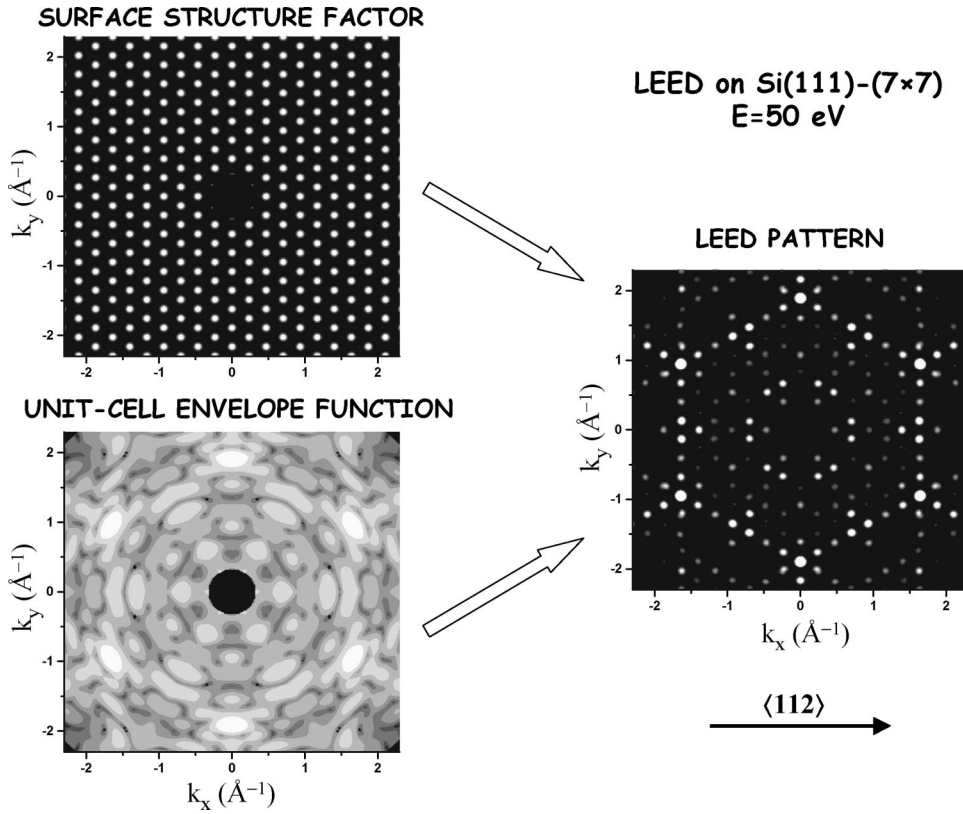## LEED on Si(111)-(7×7)
E=50 eV

LEED PATTERN

⟨112⟩

FIG. 8. Calculation of the LEED pattern of the Si(111)-(7×7) surface for 50-eV electrons coming along the surface normal. The surface structure factor S^2 (upper-left figure) has been obtained for the symmetry of the Si(111)-(7×7) surface, and for a beam diameter of 100 Å. The envelope function I (lower-left figure, on a logarithmic scale), which contains all the information about the atomic positions within a given surface unit cell as well as near-neighbor scattering, stands for the angular distribution of scattered electrons assuming that the first atomic scattering event occurs within the selected unit cell. The full LEED pattern (right figure, in linear scale) is obtained as the direct product of the structure factor and the envelope function [Eq. (38)]. The axis labels represent the components of the electron momentum parallel to the surface.

ecules. The thick solid curve represents the fully converged result obtained by using the recursion method (convergence has been obtained after 11 iterations within the scale of the figure). The thin solid curve shows the results obtained after only five iterations, which are in qualitative good agreement with the exact result. By contrast, direct Jacobi iteration is far from convergence even after 25 iterations (thick broken curve). A similar lack of convergence is also found when the SR method is used in this case. The C_{60} molecule, like the C-C cluster of Sec. IV, is a severe test of multiple scattering because the carbon atoms are reasonably strong scatterers placed relatively close together.

VI. LOW-ENERGY ELECTRON DIFFRACTION

The cluster approach followed in this work finds application in the simulation of LEED intensities for large-unit-cell surfaces, where conventional layer-by-layer schemes become quite expensive computationally. It is also directly applicable to nonperiodic surfaces, including disordered overlayers, disordered alloys, point defects, steps and kinks, adsorbed clusters, quasicrystals, etc.

In a periodic surface, the scattering of electrons in any surface unit cell differs from that of the first unit cell by a phase factor, $\exp[i(\mathbf{k}_i-\mathbf{k}_f)\mathbf{R}_a]$, where $\mathbf{k}_i$ ($\mathbf{k}_f$) is the incoming (outgoing) electron momentum vector, and $\mathbf{R}_a$ is a Bravais lattice vector. Therefore, LEED intensities can be calculated within the present cluster approach by taking ϕ_α^0 as in Eq. (37) for the atoms of the first unit cell, and zero elsewhere. One obtains

$$I_{\text{LEED}}(\Omega)=I(\Omega)|S(\mathbf{k}_i^\parallel-\mathbf{k}_f^\parallel)|^2, \qquad (38)$$

where

$$S=\sum_a e^{i(\mathbf{k}_i-\mathbf{k}_f)\mathbf{R}_a},$$

is the surface structure factor,[4] and $I(\Omega)$ is an envelope function given by Eq. (33), where the coefficients $\phi_{\alpha,L}$ are obtained from a MS calculation within a cluster containing the first unit cell and atoms around it up to a distance far enough to guarantee convergence. The cluster size is thus determined by the electron inelastic mean free path and the size of the first unit cell, with the cluster extending beyond the unit cell by roughly the electron inelastic attenuation length.

For an infinitely extended incoming beam and a perfect infinite surface, the two-dimensional structure factor S vanishes except along those directions for which the components of $\mathbf{k}_i-\mathbf{k}_f$ parallel to the surface equal a reciprocal surface lattice vector $\mathbf{G}$ denoted by Miller indices (hk), giving rise to a factor $\delta(\mathbf{k}_i^\parallel-\mathbf{k}_f^\parallel-\mathbf{G})$; this corresponds to the so-called (hk) beam at the polar direction $\Omega_\mathbf{G}$. Integrating over directions of emission around $\Omega_\mathbf{G}$, the probability that the electron is reflected along such a direction is found to be

$$P_\mathbf{G}=\left(\frac{2\pi}{Ak}\right)^2 \frac{I(\Omega_\mathbf{G})}{\cos\theta_i\cos\theta_f},$$

where θ_i (θ_f) is the polar angle of incidence (reflection) with respect to the surface normal, A is the surface unit-cell area, and k is the electron momentum. With the normalization of Eq. (37) and taking $C=1$ in Eq. (33), $P_\mathbf{G}$ is actually the fraction of incoming electrons that are reflected in the $\mathbf{G}$ beam.
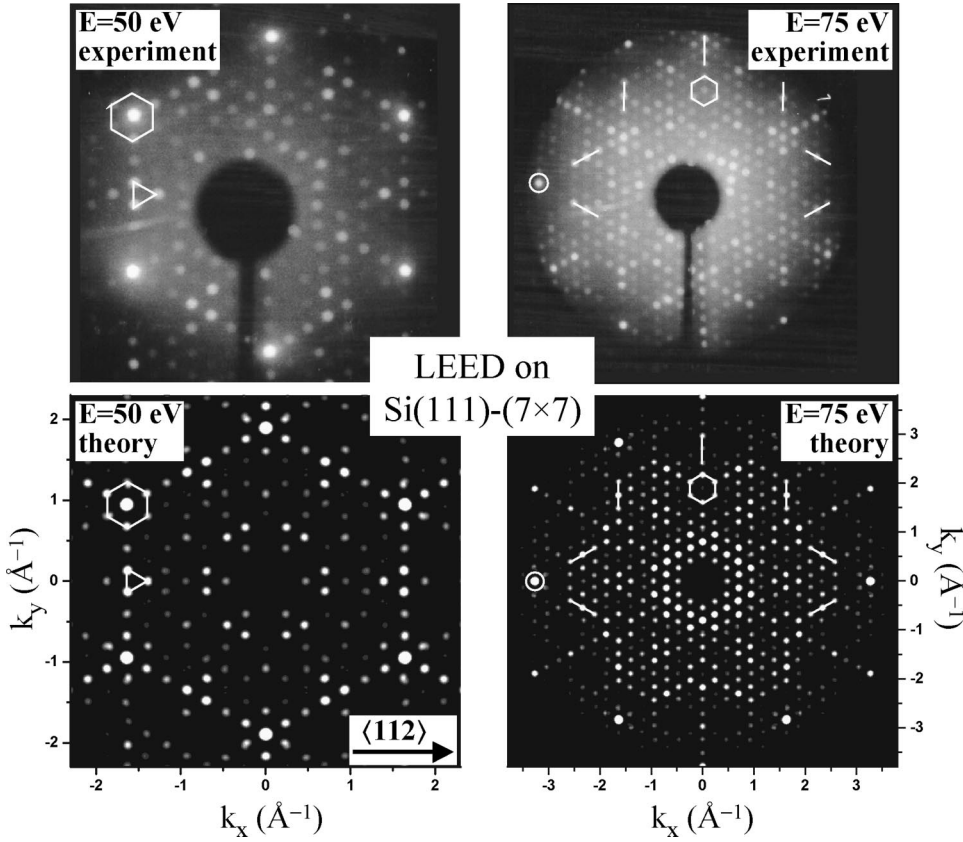
FIG. 9. Comparison of observed (upper figures, from Ref. 66) and calculated (lower figures) LEED patterns for the Si(111)-(7×7) surface using two different electron energies: 50 eV (left) and 75 eV (right). The electron beam is coming perpendicular to the surface and it has a diameter of 100 Å. The axis labels represent the components of the electron momentum parallel to the surface. Some white lines have been drawn to guide the eye.

In practice, the electron beam has a finite coherence width of the order of 100 Å, depending on the angular and energy spread of the electron gun. This effect can be accounted for in a phenomenological way by considering that only a fraction of the unit cells contribute coherently with respect to an arbitrarily chosen central unit cell. Assuming a Gaussian profile for this effect with half width H, and assuming furthermore that there is no substantial variation of coherence across any given unit cell, one finds

$$S = \sum_{\alpha} e^{-R_{\alpha}^2/2H^2} e^{i(\mathbf{k}_i - \mathbf{k}_f)\mathbf{R}_{\alpha}} = (2\pi)^3 \frac{H^2}{A} \sum_{\mathbf{G}} e^{-|\mathbf{k}_i^{\parallel} - \mathbf{k}_f^{\parallel} - \mathbf{G}|^2 H^2/2},$$
(39)

where the first (last) sum is extended over surface lattice sites $\mathbf{R}_{\alpha}$ (reciprocal surface lattice vectors $\mathbf{G}$). Obviously, the sum in reciprocal space reduces to a single term at most in the $H \to \infty$ limit, and a few more terms allow achieving good convergence for typical values of $H \sim 100$ Å. Inserting Eq. (39) into Eq. (38), one finds a finite reflection probability for every direction Ω.

The present formalism has been applied to the Si(111)-(7×7) surface. The atomic positions were taken from a previous LEED analysis,[65] in which intensive use was made of the symmetry of the surface. By contrast, the results presented here were obtained directly without any symmetry considerations beyond the surface unit-cell geometry. Figure 8 shows the final LEED pattern I_{LEED} (right figure) as well as the surface structure factor S^2 (upper left figure) and the envelope function I (lower left figure) for an incident beam of 50-eV electrons coming along the surface normal. The

axis labels represent the components of the electron momentum parallel to the surface. The structure factor exhibits a dense spot pattern that reflects the symmetry of the large unit cell of the Si(111)-(7×7) surface. This is a purely geometrical quantity which does not contain any information about the actual positions of the atoms within the surface unit cell, but does reflect the quality of the electron beam via Eq. (39). That information is fully contained in the envelope function (lower left figure), which presents marked maxima near the positions expected for the LEED spots of the unreconstructed Si(111) surface (see the six prominent peaks in the figure). The envelope function modulates the intensity that is observed around each of the spots of the structure factor, leading to the complex LEED pattern shown in the right part of the figure.

The calculation of the envelope function $I(\Omega)$ was performed using a cluster consisting of 1545 atoms, of which only 494 are contained within the surface unit cell. The cluster extends up to 15 Å below the surface, and the electron inelastic mean free path has been taken as 5.5 Å.

This calculation has been compared with experimental observations in Fig. 9 both for 50-eV electrons and for 75-eV electrons (left and right side of the figure, respectively).[66] Note the large change in the measured distribution of the brightest spots when one goes from 50 to 75 eV (upper figures), which is well reproduced by the present calculation (lower figures) using an inner potential of 10 eV.

As another example of application of the present method to LEED with a large unit cell, the case of a W(110) surface covered with one monolayer of Gd is considered in Fig. 10.
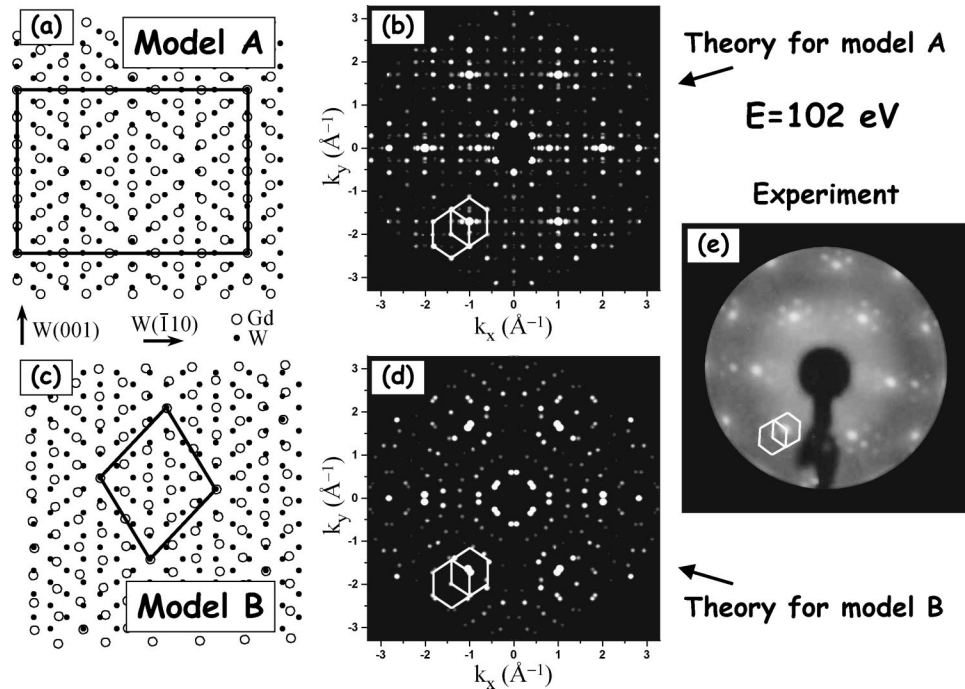
FIG. 10. (a)–(d) Calculated LEED patterns for a W(110) surface covered with one monolayer of Gd. The electron energy is 102 eV. The electron beam is coming along the surface normal and its diameter is 100 Å. (a) Schematic representation of model A for the structure with W (solid circles) and Gd (open circles) shown, leading to a large Moiré structure. (b) LEED intensity for model *A*. (c) and (d) Same as (a) and (b) for model *B*, as shown in (c). The average over the geometry depicted in (c) and its mirror reflection with respect to the W[001] direction is performed in (e). (e) Experimental result, taken from Ref. 68. The axis labels represent the components of the electron momentum parallel to the surface. Some white lines have been drawn on the LEED images to guide the eye.

Various experimental LEED studies of this structure were reported in the past.[67,68] Fig. 10(a) shows the model (*A*) proposed by Tober *et al.*,[68] wherein the Gd overlayer forms a rectangular coincidence lattice with 7×14 periodicity and with a mismatch of 0.6% area increase relative to bulk Gd(0001). The calculated LEED pattern represented in Fig. 10(b) for this model is obtained from Eqs. (38) and (39) for an electron beam diameter of 100 Å and an energy of 102 eV. The surface is described by five W layers below the Gd overlayer, so that 648 atoms are contained in the surface unit cell, and 2516 atoms are used in the calculation to include the regions surrounding the surface unit cell. Some of the spots are clearly highlighted, by the envelope function, and in particular the six brighter spots coming from the Gd overlayer. Six satellites around each of them are clearly highlighted, forming a quasisixfold satellite pattern (see the white lines drawn to guide the eye), in reasonable agreement with the experimental result shown in Fig. 10(e) (taken from Ref. 68).

Since the spot pattern imposed by *S* for this model is a rectangular one, leading to the emergence of spurious satellites not observed in the experiment, a different model structure (model *B*) with a 1.8% overall area reduction relative to Gd(0001) has been tried, as represented in Figs. 8(c) and 8(d). Two different domains are possible in this case. The corresponding LEED pattern averaged over both domains is shown in Fig. 8(d). This results in a somewhat poorer agreement with experimental observations[68] [Fig. 10(e)], and demonstrates the power of such simulations to assist in structural studies.

In summary, the present method allows one to calculate LEED patterns for complex structures using large clusters of up to several thousand atoms, which are now beyond practical reach of currently available layer-by-layer methods of LEED simulation.

VII. CONCLUSIONS

A method for the simulation of electron diffraction in atomic clusters (EDAC) was introduced. The computation time was shown to behave like $N^2(l_{max}+1)^3$, where N is the number of atoms and l_{max} is the maximum angular momentum quantum number. Actual calculations using above 1000 atoms have been presented. This was made possible via a convenient separation of the exact free-electron Green functions into rotation matrices and propagators along the *z* axis.

The resulting EDAC code relies on the iterative solution of the multiple scattering (MS) secular equation, for which various iteration techniques have been compared. In particular, the recursion method was shown to prevent eventual cases of lack of convergence in the MS expansion series and to result in faster convergence as compared with the direct MS approach. A modified recursion method was introduced in order to be able to quickly obtain angular distributions of scattered or emitted electrons from a single MS calculation (see Sec. III A).

The computational effort in EDAC is not very sensitive to the detailed form of the atomic scattering *t* matrices (e.g., diagonal vs nondiagonal), and it therefore constitutes a good

platform for including the effects of non-spherical atoms in MS. Further research in this direction is in progress.[56]

Examples of application of EDAC to PD were given for Cu(111), O/W(110), and Xe adsorbed near steps of a Pt(111) surface. The present cluster approach is particularly suitable for these cases due to the lack of translational symmetry. Also, PD from a C-C dimer was shown to lead to a lack of convergence in the MS expansion, and this pathology was prevented by using the recursion method. Electron elastic scattering on C_{60} molecules was also discussed, and MS was shown to result in improved agreement with experiment as compared to single scattering.

Finally, a formalism for studying LEED within the cluster approach was presented and applied to LEED from large-unit-cell surfaces. In particular, the relative intensity of the different LEED spots observed experimentally for the Si(111)-(7×7) are well reproduced by this theory. Also, two different models for the surface structure of one monolayer of Gd on W(110) were considered, and the resulting LEED patterns discussed in the light of the available experimental results. The formalism can also be applied to a wide variety of nonperiodic surface structures, and to free molecules.

---

*Email: jga@sc.ehu.es

[1] C. S. Fadley and S. Å. L. Bergström, Phys. Lett. A **35**, 375 (1971).

[2] A. Liebsch, Phys. Rev. Lett. **32**, 1203 (1974).

[3] S. Kono, C. S. Fadley, N. F. T. Hall, and Z. Hussain, Phys. Rev. Lett. **41**, 117 (1978); D. P. Woodruff, D. Norman, B. W. Holland, N. V. Smith, H. H. Farrell, and M. M. Traum, *ibid.* **41**, 1130 (1978); S. D. Kevan, D. H. Rosenblatt, D. Denley, B.-C. Lu, and D. A. Shirley, *ibid.* **41**, 1565 (1978); S. Kono, S. M. Goldberg, N. F. T. Hall, and C. S. Fadley, *ibid.* **41**, 1831 (1978).

[4] J. B. Pendry, *Low Energy Electron Diffraction* (Academic Press, London, 1974).

[5] M. A. Van Hove, W. H. Weinberg, and C.-M. Chan, *Low Energy Electron Diffraction* (Springer-Verlag, Heidelberg, 1986).

[6] S. A. Chambers, Adv. Phys. **40**, 357 (1991).

[7] P. A. Lee and J. B. Pendry, Phys. Rev. B **11**, 2795 (1975).

[8] J. B. Pendry, Surf. Sci. **57**, 679 (1976).

[9] C. H. Li, A. R. Lubinsky, and S. Y. Tong, Phys. Rev. B **17**, 3128 (1978).

[10] C. H. Li and S. Y. Tong, Phys. Rev. Lett. **42**, 901 (1979).

[11] J. J. Barton and D. A. Shirley, Phys. Rev. B **32**, 1906 (1985).

[12] J. J. Barton, M.-L. Xu, and M. A. Van Hove, Phys. Rev. B **37**, 10 475 (1988).

[13] J. J. Rehr and R. C. Albers, Phys. Rev. B **41**, 8139 (1990).

[14] V. Fritzsche, J. Phys.: Condens. Matter **2**, 1413 (1990).

[15] V. Fritzsche, J. Phys.: Condens. Matter **2**, 9735 (1990).

[16] D. J. Friedman and C. S. Fadley, J. Electron Spectrosc. Relat. Phenom. **51**, 689 (1990).

[17] A. P. Kaduwela, D. J. Friedman, and C. S. Fadley, J. Electron Spectrosc. Relat. Phenom. **57**, 223 (1991).

[18] J. B. Pendry, in *Determination of Surface Structure by LEED*, edited by P. M. Marcus and F. Jona (Plenum Press, New York, 1984), p. 3.

[19] D. D. Vvedensky, D. K. Saldin, and J. B. Pendry, Surf. Sci. **156**, 845 (1985).

[20] D. K. Saldin and J. B. Pendry, Surf. Sci. **162**, 941 (1985).

[21] D. K. Saldin, G. R. Harp, and X. Chen, Phys. Rev. B **48**, 8234 (1993).

[22] J. E. Müller and W. L. Schaich, Phys. Rev. B **27**, 6489 (1983).

[23] C. S. Fadley, in *Synchrotron Radiation Research: Advances in Surface and Interface Science*, edited by R. Z. Bachrach (Plenum Press, New York, 1992), p. 421.

[24] C. S. Fadley *et al.*, Prog. Surf. Sci. **54**, 341 (1997).

[25] J. L. Beeby, Proc. R. Soc. London, Ser. A **302**, 113 (1967).

[26] M. Danos and L. C. Maximon, J. Math. Phys. **6**, 766 (1965).

[27] R. Nozawa, Nucl. Instrum. Methods Phys. Res. B **100**, 1 (1966).

[28] W. L. Schaich, Phys. Rev. B **8**, 4028 (1973).

[29] C. A. Ashley and S. Doniach, Phys. Rev. B **11**, 1279 (1975).

[30] W. L. Schaich, Phys. Rev. B **29**, 6513 (1984).

[31] S. J. Gurman, N. Binsted, and I. Ross, J. Phys.: Condens. Matter **17**, 143 (1984).

[32] S. J. Gurman, N. Binsted, and I. Ross, J. Phys.: Condens. Matter **19**, 1845 (1986).

[33] J. J. Barton and D. A. Shirley, Phys. Rev. A **32**, 1019 (1985).

[34] M. Sagurton, E. L. Bullock, R. Saiki, A. Kaduwela, C. R. Brundle, C. S. Fadley, and J. J. Rehr, Phys. Rev. B **33**, 2207 (1986).

[35] J. Mustre de Leon, J. J. Rehr, C. R. Natoli, C. S. Fadley, and J. Osterwalder, Phys. Rev. B **39**, 5632 (1989).

[36] S. I. Zabinsky, J. J. Rehr, A. Ankudinov, R. C. Albers, and M. J. Eller, Phys. Rev. B **39**, 5632 (1989).

[37] A. Ankudinov and J. J. Rehr, Phys. Rev. B **52**, 10 214 (1995).

[38] G. E. Laramore, C. B. Duke, and N. O. Lipari, Phys. Rev. B **10**, 2246 (1974).

[39] C. J. Tung and R. H. Ritchie, Phys. Rev. B **16**, 4302 (1977).

[40] C. J. Powell and A. Jablonski, J. Phys. Chem. Ref. Data **28**, 19 (1999).

[41] Y. Chen, F. J. García de Abajo, A. Chassé, R. X. Ynzunza, A. P. Kaduwela, M. A. Van Hove, and C. S. Fadley, Phys. Rev. B **58**, 13 121 (1998).

[42] H. Wu and S. Y. Tong, Phys. Rev. B **59**, 1657 (1999).

[43] W. H. Press, S. A. Teukolsky, W. T. Vetterling, and B. P. Flannery, *Numerical Recipes* (Cambridge University Press, New York, 1992).

[44] R. Haydock, Solid State Phys. **35**, 215 (1980).

[45] V. Heine, Solid State Phys. **35**, 1 (1980).

[46] R. Haydock, Phys. Rev. B **61**, 7953 (2000).

[47] F. J. García de Abajo, Phys. Rev. Lett. **82**, 2776 (1999).

[48] A. Messiah, *Quantum Mechanics* (North-Holland, New York, 1966).

[49] Matrices will be represented in upper case (e.g., T) and vectors in lower case (e.g., φ^0). Spatial coordinates provide matrix and vector indices, so that products like $T\varphi^0$ involve spatial integrals: $\int d\mathbf{r}' T(\mathbf{r},\mathbf{r}')\varphi^0(\mathbf{r}')$. The unit matrix stands for $\delta(\mathbf{r}-\mathbf{r}')$, and the potential V, when understood as a matrix, represents $V(\mathbf{r})\delta(\mathbf{r}-\mathbf{r}')$.

[50] The explicit form of the coefficients $\phi^0_{\alpha,L}$ is not relevant, but the important point is that $\phi^0_\alpha(\mathbf{r})$ is a superposition of outgoing spherical waves $h^{(+)}_L[k(\mathbf{r}-\mathbf{R}_\alpha)]$ for $\mathbf{r}$ outside the muffin-tin sphere α.

[51] C. R. Natoli and M. Benfatto, J. Phys. (Paris), Colloq. **47**, C8 (1986).

[52] V. L. Shneerson, W. T. Tysoe, and D. K. Saldin, Phys. Rev. B **53**, 10 177 (1996).

[53] P. Strange, J. Staunton, and B. L. Gyorffy, J. Phys. C **17**, 3355 (1984).

[54] H. Ebert, Phys. Rev. B **38**, 9390 (1988).

[55] P. Strange, H. Ebert, J. Staunton, and B. L. Gyorffy, J. Phys.: Condens. Matter **1**, 2959 (1989).

[56] R. Díez Muiño, D. Rolles, F. J. García de Abajo, M. A. Van Hove, and C. S. Fadley (unpublished).

[57] M. Rösler and F. J. García de Abajo, Phys. Rev. B **54**, 17 158 (1996).

[58] The choice of the reliability factor R_{ave} is appropriate here, since we are comparing different theoretical calculations in which no experimental uncertainties in the zero of energy and angle scales are introduced.

[59] R. X. Ynzunza *et al.*, J. Electron Spectrosc. Relat. Phenom. **106**, 7 (2000).

[60] T. Nakatani, S. Imaga, S. Suga, Y. Kagoshima, and T. Miyahara, Jpn. J. Appl. Phys. **32**, L1480 (1993).

[61] M. A. Van Hove, A. P. Kaduwela, H. Xiao, W. Schattke, and C. S. Fadley, J. Electron Spectrosc. Relat. Phenom. **80**, 137 (1996).

[62] K. A. Thompson and C. S. Fadley, Surf. Sci. **146**, 281 (1984).

[63] V. Pouthier, C. Ramseyer, C. Girardet, K. Kuhnke, V. Marsico, M. Blanc, R. Schuster, and K. Kern, Phys. Rev. B **56**, 4211 (1997).

[64] L. G. Gerchikov, P. V. Efimov, V. M. Mikoushkin, and A. V. Solov'yov, Phys. Rev. Lett. **81**, 2707 (1998).

[65] S. Y. Tong, H. Huang, C. M. Wei, W. E. Packard, F. K. Men, G. Glandera, and M. B. Webb, J. Vac. Sci. Technol. A **6**, 615 (1987).

[66] F. J. Palomares (unpublished).

[67] J. Kolaczkiewicz and E. Bauer, Surf. Sci. **175**, 487 (1986).

[68] E. D. Tober, R. X. Ynzunza, C. Westphal, and C. S. Fadley, Phys. Rev. B **53**, 5444 (1996).